

Numerical Simulations and Experimental Validation on LBW Bead Profiles of Ti-6Al-4V Alloy

Harish Mooli, Srinivasa Rao Seeram, Satyanarayana Goteti and Nageswara Rao Boggarapu*

Department of Mechanical Engineering, Koneru Lakshmaiah Education Foundation, Deemed to be University, Green Fields, Vaddeswaram, Guntur-522 502, India

ABSTRACT

The lightweight titanium alloys possess good resistance to corrosion and temperature. They are used in turbine engines and aircraft structures. The strength of weld joint is dependent on thermal history in the weld zone and the weld bead geometry. The quality of weld can be improved by specifying the optimal welding parameters. Trial-and-error experimental methods are time-consuming and expensive. This paper deals with Computational Fluid Dynamics (CFD) models to carry out three-dimensional thermo-fluid analysis. Buoyancy and Marangoni stress are incorporated. Temperature dependent properties of Ti-6Al-4V alloy and the process conditions are specified for generating the weld bead profile. The CFD model is validated initially through comparison of existing test data. Further studies are made by conducting tests on the pulsating laser welding of Ti-6Al-4V alloy. The effects of welding speed, pulse width and pulse frequency on the weld bead geometry are examined. This study confirms the adequacy of modeling and simulations of weld bead geometry with test results.

Keywords: Beam diameter, frequency, power, pulse width, weld bead

ARTICLE INFO

Article history:

Received: 06 February 2021

Accepted: 02 April 2021

Published: 31 July 2021

DOI: <https://doi.org/10.47836/pjst.29.3.32>

E-mail addresses:

harish.m313@gmail.com (Harish Mooli)

ssrao@kluniversity.in (Srinivasa Rao Seeram)

gotetisatya@yahoo.co.in (Satyanarayana Goteti)

bnrao52@rediffmail.com (Nageswara Rao Boggarapu)

* Corresponding author

INTRODUCTION

Welding is one of the critical technologies in most of the relevant engineering applications. Gas Tungsten Arc Welding (GTAW) and Electron Beam Welding (EBW) are widely being used in aerospace, automotive, chemical, food, medical and nuclear industries. Laser Beam Welding (LBW), a fusion joining technique, is

characterized by small Heat Affected Zone (HAZ) and Fusion Zone (FZ), and minimal distortion. Advanced research is directed towards development of modeling and simulation tools, in addition to the process control in welding metallurgy (Wu et al., 2018; Ruan et al., 2018; Dal & Peyre, 2017; D'Ostuni et al., 2017; Popescu et al., 2017). Extensive studies are made on laser weld joint properties of metallic materials such as Al-based alloys (Zhang et al., 2017), AZ31 alloy (Lu et al., 2018), Al-steel (Cui et al., 2017; Casalino et al., 2017), steels (Górka & Stano, 2018; Mohammed et al., 2017; Xue et al., 2017; Evin & Tomáš, 2017), and Ti-based alloys (Zeng et al., 2017; Sánchez-Amaya et al., 2017; Caiazzo et al., 2017b). Mashinini & Hattingh (2018) have utilized LBW for joining 3 mm thick Ti-6Al-4V alloy sheets. Chmelíčková et al. (2020) have characterized butt welds of Ti-6Al-4V alloy sheets. Welding has been performed using a pulsed Neodymium-doped Yttrium Aluminum Garnet (Nd:YAG) laser under argon shielding gas atmosphere. The effects of LBW processes for titanium alloys are examined on weld pool shape, bead width, HAZ and other weld bead characteristics.

Kumar et al. (2017) have performed LBW of Ti-6Al-4V alloys in butt configurations. Rajulu et al. (2018) have conducted experiments to examine the weld bead characteristics considering the process variables (such as pulse frequency, pulse width, welding speed, and pulse energy). Empirical relations are developed using response surface methodology (RSM) for the bead geometry in terms of the process variables. Caiazzo et al. (2017a) have conducted number of weld trials on Ti-6Al-4V plates in corner joint followed by microstructure and microhardness tests. Optimal LBW process variables are identified with minimal undercut and porosity. Liu et al. (2014) have made the fatigue damage evolution on pulsating laser welding of Ti-6Al-4V alloy. Amaya et al. (2013) have observed fine grain microstructure by low heat input causing enhancement in the critical nominal strain delaying crack-initiation. Cai et al. (2017) have used pure Ti-filler with laser to improve the welding properties of γ -Ti-Al alloy. Boccarusso et al. (2015) have examined the influence of LBW parameters on defects in Ti-6Al-4V hot rolled sheets. Junaid et al. (2017) have performed pulsating laser welding of Ti-5Al-2.5Sn alloy to examine the effect of LBW parameters on weld pool shape, pulse overlap, oxide formation and microstructure (using Scanning Electron Microscope (SEM) and Optical Microscope (OM)). Laser peak power indicates significant effects on the FZ oxygen contents and grain size. Weld pool shape is controlled by the peak power and heat input per unit length. Kashaev et al. (2016) have analyzed the morphology of butt and T-joints in LBW of Ti-6Al-4V alloy and achieved low porosity in the desired seam geometry. Hong and Shin (2016) have adopted a multi-physics prediction model to analyze the bead profile and properties in laser welding of Ti-6Al-4V alloy.

The strength of weld joint is dependent on thermal history in the weld bead geometry. To improve the quality of weld, there is a need for specifying the optimal welding parameters.

Time consuming trial-and-error approaches are expensive. Computational welding mechanics (CWM) has become an active field in the Welding Science and Technology. However, use of CWM in industries is in the initial stage. A CFD model for 3D thermo-fluid analysis is developed incorporating the buoyancy and Marangoni stress. Temperature dependent properties including the process conditions are specified for estimating the weld bead profile. The CFD model is validated initially through comparison of existing test data. Later on, tests are conducted for further validation of the developed model on the pulsating laser welding of Ti-6Al-4V alloy. The influence of welding speed, pulse width and pulse frequency on weld bead geometry are investigated. The test results are compared with three dimensional unsteady numerical simulations.

MATERIALS AND METHODS

Titanium alloys are light in weight and possess good resistance to corrosion and temperature. Welding tests are conducted with pulsed laser beam on Ti-6Al-4V alloy to study the weld pool geometry. A three-dimensional fluid flow and heat transfer model is developed for generation of weld bead geometry using a volumetric laser heat source. Details on the model development and welding process simulations using Ansys 16 fluent are presented below. This section also highlights the validity of numerical simulations with test results.

Thermo-fluid Analysis

In laser welding, thermo-fluid phenomena were examined by integrating the user defined functions with the code of finite volume method in ANSYS and solving the Navier–Stokes and the k - ε equations in mushy zone and regions of weld pool as in Equation 1 (Satyanarayana et al., 2018; Satyanarayana et al., 2019a; Satyanarayana et al., 2019b).

The continuity equation is:

$$\frac{\partial \rho}{\partial t} + \nabla \cdot (\rho \vec{V}) = 0 \quad [1]$$

Here ρ , t and \vec{V} are the density, time and the weld pool velocity respectively.

The density (ρ) and the liquid mass fraction (f_L) are defined in Equation 2 and 3:

$$\rho = f_L \rho_L + f_S \rho_S = f_L \rho_L + (1 - f_L) \rho_S \quad [2]$$

$$\begin{aligned} f_L &= 0 \quad \text{for } T \leq T_S \\ &= (T - T_S)(T_L - T_S)^{-1} \quad \text{for } T \in [T_S, T_L] \\ &= 1 \quad \text{for } T \geq T_L \end{aligned} \quad [3]$$

The momentum Equation 4 is as below (ANSYS, 2013; ANSYS, 2016):

$$\frac{\partial(\rho\vec{V})}{\partial t} + \nabla \cdot (\rho\vec{V}\vec{V}) = -\nabla p + \mu \nabla^2 \vec{V} + \rho\vec{g} + \vec{S}_w \quad [4]$$

Here p , μ and $\rho\vec{g}$ are the static pressure, viscosity, and the gravitational body force.

Denoting A_{mush} as the mushy zone constant and \vec{w} as the pull velocity, the source term (or momentum frictional dissipation) in the mushy zone is expressed as Equation 5 (Voller & Prakash, 1987; Brent et al., 1988)

$$\vec{S}_w = (f_L^3 + 10^{-3})^{-1} (1 - f_L)^2 (\vec{w}) A_{mush} \quad [5]$$

The enthalpy-porosity technique of Jalali and Najafi (2010) is adopted to identify the interface from the phase change.

The energy Equation 6 is:

$$\frac{\partial(\rho H)}{\partial t} + \nabla \cdot (\rho\vec{V}H) = \nabla \cdot (\kappa \nabla T) + S \quad [6]$$

Here $H (\equiv h + \Delta H)$, $h \left(= h_{ref} + \int_{T_{ref}}^T C_p dT \right)$ and S are the enthalpy, sensible heat, and volumetric heat source, respectively. C_p , h_{ref} and κ are respectively, the specific heat, reference enthalpy and thermal conductivity.

The latent heat (ΔH) for a solid is zero, whereas in case of a liquid (Equation 7),

$$\Delta H = m_L L \quad [7]$$

Here L is the latent heat of the liquid metal. Top surface of the flat weld pool normal velocity is zero.

The shearing stress (Equation 8),

$$\tau = \frac{\partial \sigma}{\partial T} \nabla T \quad [8]$$

The lumped convection coefficient (Akbari et al., 2014): $h_c = 2.4 \times 10^{-3} \varepsilon T^{1.61}$ is used for imposing conditions of convection and radiation on all surfaces. Due to laser, a transient heat flux is considered on the top surface.

Introducing the Stefan–Boltzmann constant (σ_{SB}), emissivity (ε), and the ambient temperature (T_a), the energy balance is of the form (Equation 9) (Satyanarayana, 2020):

$$\kappa \frac{\partial T}{\partial z} = q - h_c (T - T_a) - \sigma_{SB} \varepsilon (T^4 - T_a^4) \quad [9]$$

For laser, the volumetric heat flux (q_v) is a Gaussian distribution of the form (Equation 10).

$$q_v = \frac{2P}{\pi r_0^2 \delta} i(t) \exp\left(1 - \frac{r^2}{r_0^2}\right) \left(1 - \frac{y}{\delta}\right) \quad [10]$$

Here P is the absorbed laser power. The current radius (r) is from cone axis. r_0 is the radius of laser beam. y is the depth and δ is the thickness. In pulsed laser welding, the time-based function, $i(t) = 1$, when the pulse is active, whereas $i(t) = 0$, when the pulse is inactive.

Model is developed for fluid flow and heat transfer using Ansys16 Fluent as in (Satyanarayana et al., 2018; Satyanarayana et al., 2019a; Satyanarayana et al., 2019b). User defined functions (UDF) are embedded. Residual stresses can be evaluated by exporting the thermal history from CFD analysis to Ansys16 FEA solver. Procedure for welding process simulations is highlighted briefly below:

- Step-1:** Creation of the computational domain and component geometry.
- Step-2:** Creation of fine and coarse meshes near and away from heat source.
- Step-3:** Selection of phases and turbulence models.
- Step-4:** Introduction of user defined codes (UDFs).
- Step-5:** Specification of thermal and physical material properties.
- Step-6:** Application of boundary conditions.
- Step-7:** Specification of number of time steps and iterations (solution convergence including welding and cooling phase).
- Step-8:** Laser beam activation with starting and end positions.
- Step-9:** Acquiring information on temperature and fluid flows.
- Step-10:** Increase the time step to improve the solution. Otherwise, move to Step-12
- Step-11:** Change of laser beam position proceed to Step-9
- Step-12:** Record the weld bead profile and temperature distribution;
- Step-13:** Export the geometry and solution files from Fluent to Finite Element Analysis (FEA) solver.
- Step-14:** Specification of reference temperature, mechanical properties to FEA solver.
- Step-15:** Check the mesh configuration
- Step-16:** Import thermal loads from CFD to FEA
- Step-17:** Application of structural boundary conditions
- Step-18:** Solving for stress and strain in the weld coupon.
- Step-19:** Increase in time-step for the incompleteness of job. Otherwise go to Step-21.

Step-20: To simulate transient state, the previous time step results are applied as initial conditions and go to Step-18.

Step-21: Record the results. Stop numerical simulations.

The above procedure is followed to examine the impact of thermo-physical properties on various performance indicators. This paper presents CFD analysis results for checking the adequacy of the weld bead profiles.

Validity of Numerical Simulations

Numerical simulations are performed on pulsed laser welding to examine the adequacy of the developed 3D flow model through comparison with existing test data. Jiang et al. (2019) have conducted pulsed laser welding on 50 × 20 × 3 mm Ti-6Al-4V alloy plates. Table 1 gives specifications of machine configurations.

Table 1
Details on the pulsed laser welding of 3mm thick Ti-6Al-4V alloy (Jiang et al., 2019)

S. No.	Machine Specifications	
1	Laser source	Nd:YAG pulsed IQL-20
2	Maximum power	750W
3	Pulse wavelength	1.06
4	Laser variable range	0.2 to 25ms
5	Pulse frequency	1-250 Hz
6	Pulse energy	0 to 40J
7	Spot diameter	0.7mm
8	Focal distance	6mm

The following temperature dependent properties as in (Rai, 2008) are considered in the present numerical simulations. Specific heat of solid is 670 J/kg K, whereas it is 730 J/kg K in liquids. Viscosity of liquid is 0.005 kg/m.s. Melting heat is 370000 J/kg. Solidus temperature is 1878 K. Liquidus temperature is 1928 K.

The density, $\rho(\text{kg/m}^3)$ in terms of temperature, $T(K)$ is defined in Equation 11 and 12.

$$\rho_s = 4420 - 0.154(T - 300) \tag{11}$$

$$\rho_L = 3920 - 0.68(T - 1928) \tag{12}$$

Thermal conductivity, $\kappa(W.m^{-1}.K^{-1})$ in terms of temperature, $T(K)$ is defined as Equation 13.

$$\begin{aligned} \kappa &= -0.32 + 1.46 \times 10^{-2} T \quad \text{for } 1400 < T < 1850K \\ &= -6.66 + 1.83 \times 10^{-2} T \quad \text{for } 1950 < T < 2700K \end{aligned} \tag{13}$$

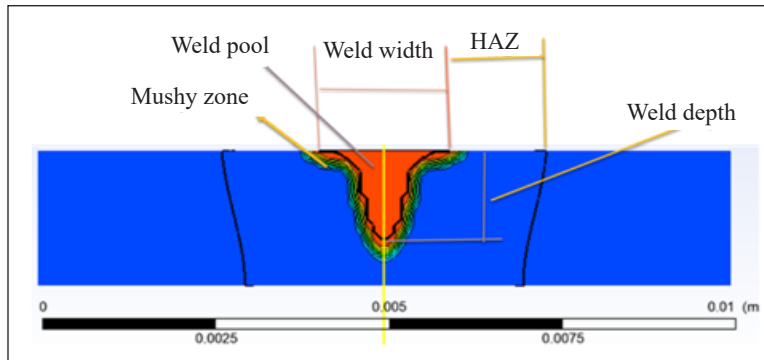


Figure 1. Nomenclature of the weld bead profile

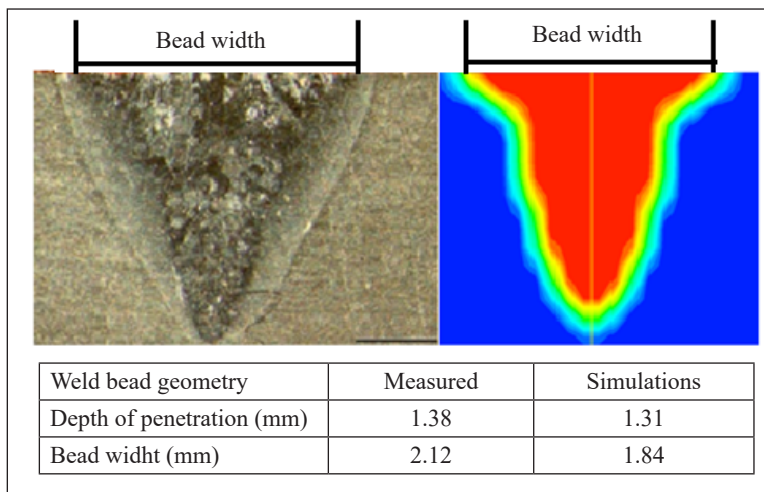


Figure 2. Comparison of simulated weld bead geometry with the test result (Jiang et al., 2019)

Following the procedure in the preceding section for laser welding process simulations on Ti-6Al-4V alloy, weld pool cross-section is generated at the 240W of average power, 25Hz frequency, 4.2 ms pulse width and 0.7mm beam diameter. Figure 1 shows the nomenclature of CFD simulation weld bead profile. Figure 2 shows the comparison of the experimental and numerical CFD simulations of the weld bead profile. Numerical simulation results in Figure 2 indicate the validity with test data (Jiang et al., 2019).

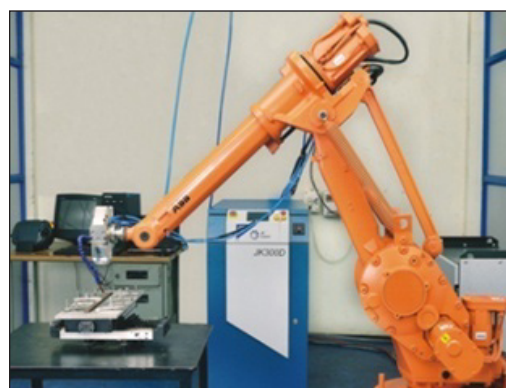


Figure 3. Experimental set-up for pulsed LBW of Ti-6Al-4V alloy

Experiments are performed to examine the adequacy of the temperature dependent properties, modeling, and numerical simulations of pulsated laser beam welding of Ti-6Al-4V alloy. A 16kW Nd:YAG pulsed mode integrated with CNC (Computer Numerical Control) station is used. Figure 3 shows the experimental set-up. Pulsated laser welding has been carried out on 50 × 20 × 2 mm Ti-6Al-4V alloy plates. Butt joint is the configuration. The laser heat source moves along the direction of work-piece length. The workpiece is supported by clamping device to minimize distortion and displacement. Ti-6Al-4V alloy contains highly oxidized elements.

RESULTS AND DISCUSSION

During welding, there is a possibility of oxidation under atmospheric condition. Shielding gas argon is used to overcome such problems. Pulse frequency (Hz), pulse width (ms), pulse energy (J) and beam diameter (mm) are strongly related with each other (Equation 14 & 15). Table 2 gives the input variables for three test runs.

$$Pulse\ energy\ (J) = \frac{Average\ Power(W)}{Frequency\ (Hz)} \tag{14}$$

$$Peak\ power\ (W) = \frac{Pulse\ energy}{pulse\ width} \tag{15}$$

Table 2
Input variables considered in the pulsated LBW Process

Test Run	Frequency (Hz)	Pulse Width (ms)	Pulse Energy (J)	Average Power (W)	Peak Power (W)	Speed (mm/s)
1	16	9	14	224	1556	2.0
2	14	8	20	280	2550	1.5
3	16	7	14	224	2000	1.0

The weld pool shape for test run-1 is shown in Figure 4. The simulated weld bead geometry is compared with the test run-1 in Figure 5. Temperature distribution is shown in Figure 6. The velocity contour plot in the weld pool is shown in Figure 7.

Peclet number $P_e = \frac{L_R C_p \rho u}{\kappa}$ indicates the relative rate of heat transfer (by convection and conduction). Here, u is the weld pool velocity. ρ , C_p , κ and L_R are respectively, the liquid density, specific heat, liquid metal thermal conductivity and the pool radius. In the present study, $P_e > 5$. This indicates convective heat transfer domination over conduction mode. The heat transfer is due to convection in weld pool. The molten weld pool moves

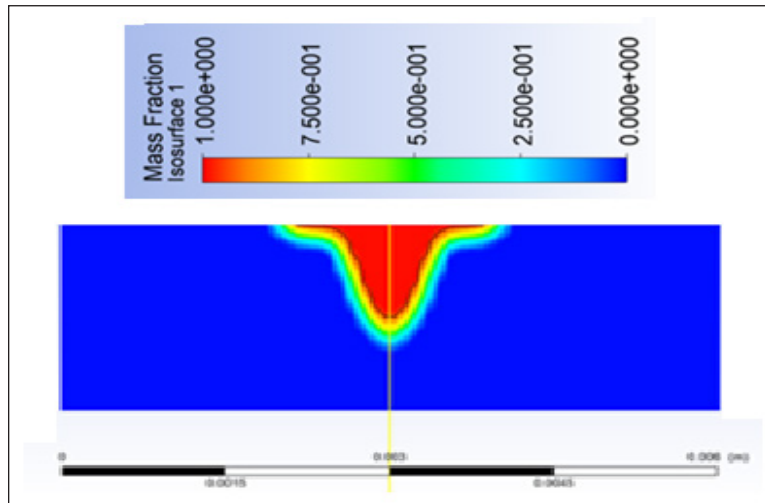


Figure 4. Weld pool shape for test run-1

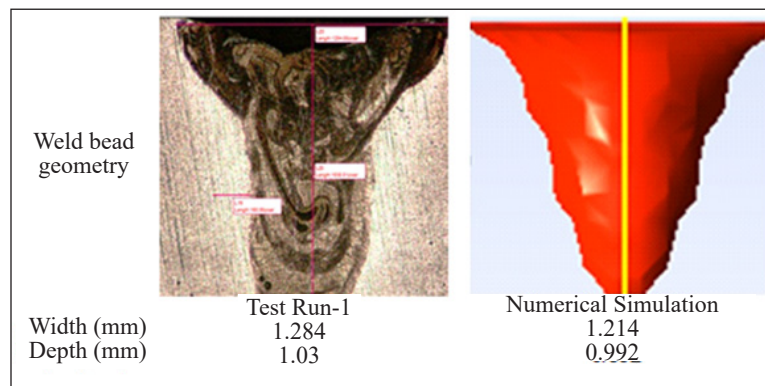


Figure 5. Comparison of simulated weld bead geometry with test run-1

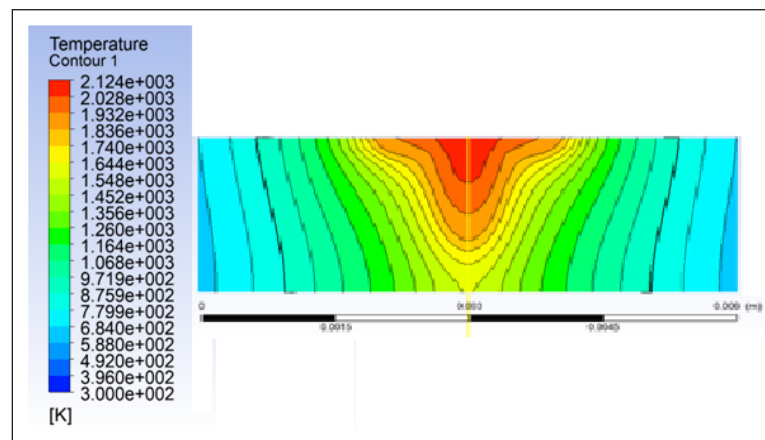


Figure 6. Temperature distribution (test run-1: pulse width= 9 ms; welding speed=2 mm/s)

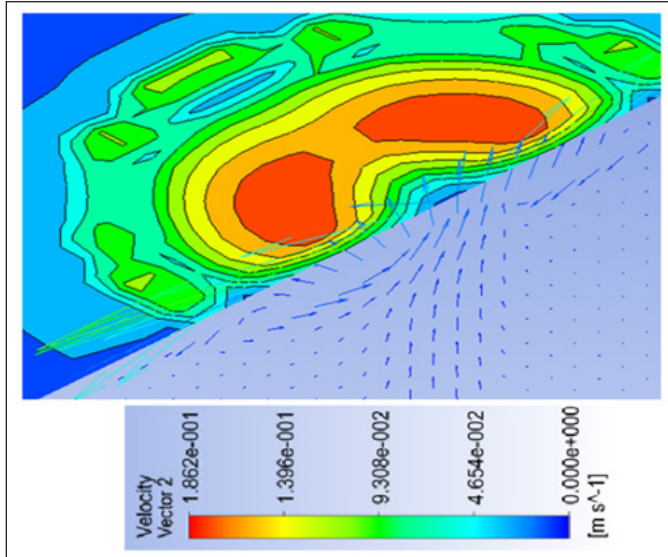


Figure7. Velocity contour plot in the weld pool (test run-1)

from inward to top (or reverse in direction), which depends on the surface tension gradient on pool top surface. The convective movement influences the weld geometry.

Marangoni and buoyancy are driving forces in the weld pool flow. Marangoni (Ma) and Grashof (Gr) numbers show the importance of these forces (Equation 16 & 17).

$$Ma = \frac{\rho L_R}{\mu^2} \frac{\partial \sigma}{\partial T} \Delta T \quad [16]$$

$$Gr = g \rho^2 \beta L_B^3 \frac{\Delta T}{\mu^2} \quad [17]$$

Here g is the gravitational acceleration. ΔT is the difference in weld pool and solidus peak temperatures. L_B is the characteristic length for the buoyancy force in the liquid pool. It is approximately $\frac{1}{8}$ of the weld pool width (Debroy & David, 1995). In this present case study, Ma/Gr is in the order of 10^5 . Hence, the weld pool flow is driven by surface tension gradient.

Figure 8 shows simulated weld bead geometry for test run-2. The temperature distribution is shown in Figure 9. For test run-3, weld bead geometry and temperature distribution are shown in Figures 10 and 11, respectively. Numerical simulations of the weld bead profiles are close to the ones observed from tests. This demonstrates the validity of modeling and specification of temperature dependent properties. Temperature distribution will be useful to estimate residual stress in weld-joints from FEA. Experiments

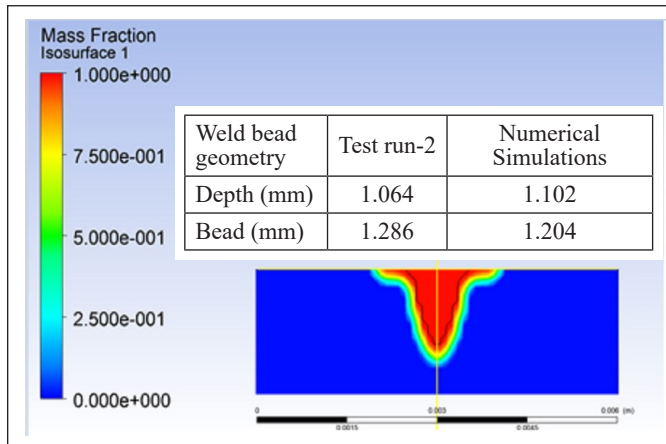


Figure 8. Weld pool shape for pulse width 8 ms and welding speed 1.5 mm/s

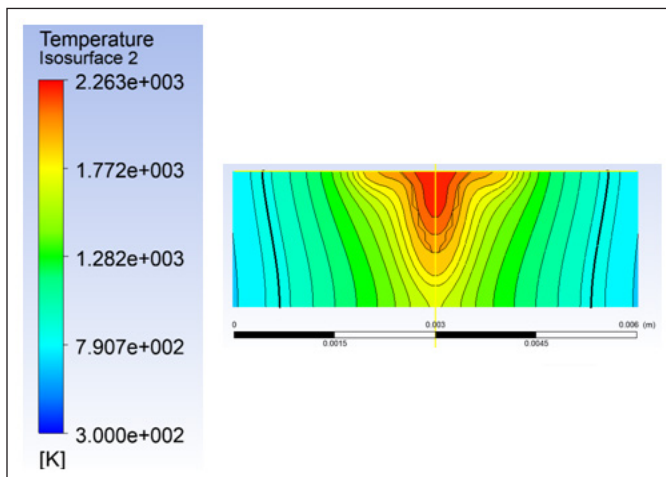


Figure 9. Temperature distribution for test run-2 (pulse width= 8 ms; welding speed= 1.5 mm/s)

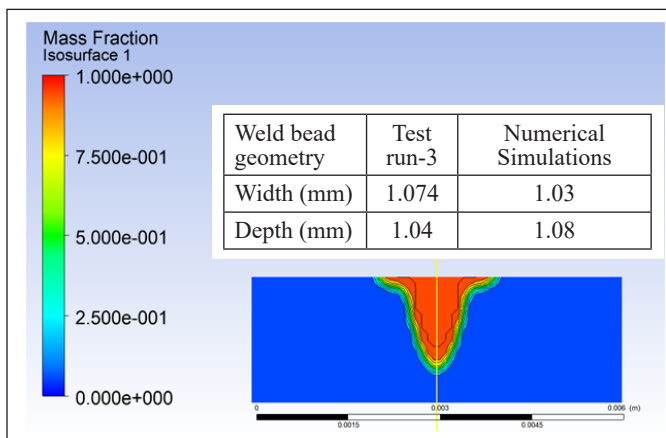


Figure 10. Weld pool shape for pulse width 7 ms and welding speed 1.0 mm/s

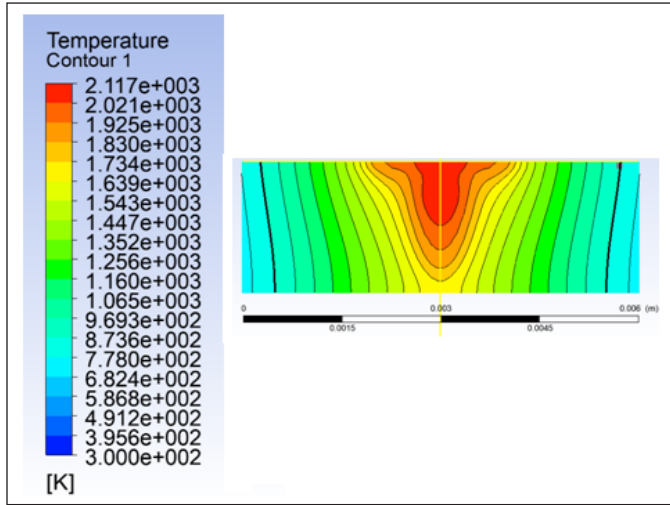


Figure 11. Temperature distribution for test run-3 (pulse width= 7 ms; welding speed= 1.0 mm/s)

are conducted to study the impact of frequency on weld pool dimensions at constant speed, pulse width and pulse energy varying frequency from 12 to 16 Hz. Both weld width and depth are increased (Table 3). The quality of weld depends on heat transfer process, power density and interaction time (Equation 18 & 19).

$$Power\ density = \frac{Laser\ power}{Area\ of\ laser\ beam} \quad [18]$$

$$Interaction\ time = \frac{Beam\ Diameter}{Welding\ speed\ of\ the\ laser\ beam\ source\ and\ heat\ transfer} \quad [19]$$

The Laser power is increased with increasing the frequency; the plate receives high energy for the interaction time causing increase in the absorbed energy by melting pool and its temperature. This results in high weld width and depth. The test results of Table 4 confirm the effect of pulse energy. Tests are conducted by doubling the welding speed keeping other parameters constant. This reduces the interaction time of the laser beam to half. When the welding speed is increased test results in Table 5 indicate increase in

Table 3
Weld bead geometry with varying frequency

Test Run	Frequency (Hz)	Pulse width (ms)	Pulse Energy(J)	Average Power(W)	Peak Power(W)	Speed (mm/s)	Weld Width (mm)	Weld Depth (mm)
4	12	9	14	168	1556	1	1.05	0.68
5	16	9	14	224	1556	1	1.314	0.98

Table 4
Weld bead geometry with varying pulse energy

Test Run	Frequency (Hz)	Pulse width (ms)	Pulse Energy(J)	Average Power(W)	Peak Power(W)	Speed (mm/s)	Weld Width (mm)	Weld Depth (mm)
6	14	8	16	224	2000	1.5	0.916	0.476
7	14	8	20	280	2550	1.5	1.064	1.286

Table 5
Weld bead geometry with varying weld speed

Test Run	Frequency (Hz)	Pulse width (ms)	Pulse Energy(J)	Average Power(W)	Peak Power(W)	Speed (mm/s)	Weld Width (mm)	Weld Depth (mm)
8	12	9	18	216	2000	1	1.056	1.292
9	12	9	18	216	2000	2	1.264	0.774

weld width and decrease in depth. The width of melting is increased due to reducing heat interaction time and aggregation of melted material in the upper layer. It should be noted that frequency, pulse energy and welding speed are the welding parameters controlling bead width. These three parameters are commonly known to affect the weld bead. Though the frequency and pulse energy are same for the bead widths of test run-1 and test run-3 (Figures 5 and 10), the high welding speed reduces the heat input to the bead resulting reduction in the width and depth of penetration. But only penetration was narrow for test run-1 as compared to test run-3. This may be due to high welding speed and pulse width with low peak power in test run-1. In general, the width of melting is increased because less penetration laser beam to the lower layers due to reducing heat interaction time and aggregation of melted material in the upper layer.

CONCLUSIONS

Welding tests are conducted with pulsed laser beam on Ti-6Al-4V alloy to study the weld pool geometry. A three-dimensional fluid flow and heat transfer model is developed for generation of the weld bead geometry, temperature and velocity contours in the weld pool using a volumetric laser heat source. The major findings are:

- Numerical simulations are comparable with the results of existing and conducted experiments.
- Convection heat transfer is the major process in weld pool shape formation.
- The temperature gradient on the weld pool top surface plays a major role.
- The weld pool size depends on the power density and interaction time. High power density and low interaction time result in high weld depth and low weld width.
- High frequency increases the weld pool volume.

Modeling and simulations will be useful in generating the weld geometry and temperature profiles in FZ and HAZ. It is possible to control the laser welding parameters for achieving optimal weld pool geometry and to minimize the developmental cost for new applications. It is planned to adopt the Taguchi design of experiments, which will minimize the number of numerical simulations and provide information for full factorial design of experiments. Multi-objective optimization concepts can be utilized to select the optimal LBW parameters for achieving narrow weld bead width with full depth of penetration.

ACKNOWLEDGEMENTS

The authors wish to acknowledge greatly to Optilase, India's first Laser Process Development center, SIDCO Women's Industrial Estate, Thirumullaivoyal, Chennai – 600 062 Tamilnadu, India, for providing facilities to carry out the experimental studies. Finally, the authors are grateful to the reviewers for their constructive criticism to improve the clarity of presentation.

REFERENCES

- Akbari, M., Saedodin, S., Toghraie, D., Shoja-Razavi, R., & Kowsari, F. (2014). Experimental and numerical investigation of temperature distribution and melt pool geometry during pulsed laser welding of Ti6Al4V alloy. *Optics & Laser Technology*, 59, 52-59. <https://doi.org/10.1016/j.optlastec.2013.12.009>
- Amaya, J. S., Amaya-Vázquez, M. R., & Botana, F. J. (2013). Laser welding of light metal alloys: Aluminium and titanium alloys. In *Handbook of Laser Welding Technologies* (pp. 215-254). Woodhead Publishing. <https://doi.org/10.1533/9780857098771.2.215>
- ANSYS. (2013). *ANSYS fluent theory guide*. ANSYS Inc.
- ANSYS. (2016). *ANSYS® academic research, release 16.0, ANSYS Fluent in ANSYS Workbench User's Guide*. ANSYS Inc.
- Boccarusso, L., Arleo, G., Astarita, A., Bernardo, F., de Fazio, P., Durante, M., Giudice, G., Minutolo, F. M. C., Sepe, R., & Squillace, A. (2015). Effect of the process parameters on the geometrical defects of Ti-6Al-4V hot rolled sheets laser beam welded. In *Key Engineering Materials* (Vol. 651, pp. 901-906). Trans Tech Publications Ltd. <https://doi.org/10.4028/www.scientific.net/KEM.651-653.901>
- Brent, A. D., Voller, V. R., & Reid, K. T. J. (1988). Enthalpy-porosity technique for modeling convection-diffusion phase change: application to the melting of a pure metal. *Numerical Heat Transfer, Part A Applications*, 13(3), 297-318. <https://doi.org/10.1080/10407788808913615>.
- Cai, X., Sun, D., Li, H., Guo, H., Gu, X., & Zhao, Z. (2017). Microstructure characteristics and mechanical properties of laser-welded joint of γ -TiAl alloy with pure Ti filler metal. *Optics & Laser Technology*, 97, 242-247. <https://doi.org/10.1016/j.optlastec.2017.07.011>.
- Caiazza, F., Alfieri, V., Corrado, G., Argenio, P., Barbieri, G., Acerra, F., & Innaro, V. (2017a). Laser beam welding of a Ti-6Al-4V support flange for buy-to-fly reduction. *Metals*, 7(5), Article 183. <https://doi.org/10.3390/met7050183>

- Caiazzo, F., Alfieri, V., Astarita, A., Squillace, A., & Barbieri, G. (2016b). Investigation on laser welding of Ti-6Al-4V plates in corner joint. *Advances in Mechanical Engineering*, 9(1). <https://doi.org/10.1177/1687814016685546>
- Casalino, G., Leo, P., Mortello, M., Perulli, P., & Varone, A. (2017). Effects of laser offset and hybrid welding on microstructure and IMC in Fe–Al dissimilar welding. *Metals*, 7(8), Article 282. <https://doi.org/10.3390/met7080282>.
- Chmelíčková, H., Hiklová, H., Václavek, L., Tomáščík, J., & Čtvrtlík, R. (2020). Characterization of titanium laser welds. *Acta Polytechnica CTU Proceedings*, 27, 145-148. <https://doi.org/10.14311/APP.2020.27.0145>.
- Cui, L., Chen, B., Qian, W., He, D., & Chen, L. (2017). Microstructures and mechanical properties of dissimilar Al/Steel butt joints produced by autogenous laser keyhole welding. *Metals*, 7(11), Article 492. <https://doi.org/10.3390/met7110492>.
- D'Ostuni, S., Leo, P., & Casalino, G. (2017). FEM simulation of dissimilar aluminum titanium fiber laser welding using 2D and 3D Gaussian heatsources. *Metals*, 7(8), Article 307. <https://doi.org/10.3390/met7080307>.
- Dal, M., & Peyre, P. (2017). Multiphysics simulation and experimental investigation of aluminum wettability on a titanium substrate for laser welding-brazing process. *Metals*, 7(6), Article 218. <https://doi.org/10.3390/met7060218>.
- DebRoy, T., & David, S. A. (1995). Physical processes in fusion welding. *Reviews of Modern Physics*, 67(1), Article 85. <https://doi.org/10.3390/met7110504>.
- Evin, E., & Tomáš, M. (2017). The influence of laser welding on the mechanical properties of dual phase and TRIP steels. *Metals*, 7(7), Article 239. <https://doi.org/10.3390/met7070239>
- Górka, J., & Stano, S. (2018). Microstructure and properties of hybrid laser arc welded joints (laser beam-mag) in thermo-mechanical control processed S700MC steel. *Metals*, 8(2), Article 132. <https://doi.org/10.3390/met8020132>.
- Hong, K. M., & Shin, Y. C. (2016). Analysis of microstructure and mechanical properties change in laser welding of Ti6Al4V with a multiphysics prediction model. *Journal of Materials Processing Technology*, 237, 420-429. <https://doi.org/10.1016/j.jmatprotec.2016.06.034>.
- Jalali, A., & Najafi, A. F. (2010). Numerical modeling of the solidification phase change in a pipe and evaluation of the effect of boundary conditions. *Journal of Thermal Science*, 19(5), 419-424. <https://doi.org/10.1007/s11630-010-0403-z>.
- Jiang, D., Alsagri, A. S., Akbari, M., Afrand, M., & Alrobaian, A. A. (2019). Numerical and experimental studies on the effect of varied beam diameter, average power and pulse energy in Nd: YAG laser welding of Ti6Al4V. *Infrared Physics & Technology*, 101, 180-188. <https://doi.org/10.1016/j.infrared.2019.06.006>.
- Junaid, M., Khan, F. N., Rahman, K., & Baig, M. N. (2017). Effect of laser welding process on the microstructure, mechanical properties and residual stresses in Ti-5Al-2.5 Sn alloy. *Optics & Laser Technology*, 97, 405-419. <https://doi.org/10.1016/j.optlastec.2017.07.010>.

- Kashaev, N., Ventzke, V., Fomichev, V., Fomin, F., & Riekehr, S. (2016). Effect of Nd: YAG laser beam welding on weld morphology and mechanical properties of Ti–6Al–4V butt joints and T-joints. *Optics and Lasers in Engineering*, 86, 172-180. <https://doi.org/10.1016/j.optlaseng.2016.06.004>.
- Kumar, C., Das, M., Paul, C. P., & Singh, B. (2017). Experimental investigation and metallographic characterization of fiber laser beam welding of Ti-6Al-4V alloy using response surface method. *Optics and Lasers in Engineering*, 95, 52-68. <https://doi.org/10.1016/j.optlaseng.2017.03.013>.
- Liu, J., Gao, X. L., Zhang, L. J., & Zhang, J. X. (2014). A study of fatigue damage evolution on pulsed Nd: YAG Ti6Al4V laser welded joints. *Engineering Fracture Mechanics*, 117, 84-93. <https://doi.org/10.1016/j.engfracmech.2014.01.005>.
- Lu, G. F., Zhang, L. J., Pei, Y., Ning, J., & Zhang, J. X. (2018). Study on the size effects of H-Shaped fusion zone of fiber laser welded AZ31 joint. *Metals*, 8(4), Article 198. <https://doi.org/10.3390/met8040198>.
- Mashinini, P. M., & Hattingh, D. G. (2018). Influence of Laser Power and Traverse Speed on Weld Characteristics of Laser Beam Welded Ti-6Al-4V Sheet. *Mechanical Stress Evaluation by Neutron and Synchrotron Radiation: MECA SENS 2017*, 4(2018), 59-64. <http://dx.doi.org/10.21741/9781945291678-9>
- Mohammed, G. R., Ishak, M., Ahmad, S. N. A. S., & Abdulhadi, H. A. (2017). Fiber laser welding of dissimilar 2205/304 stainless steel plates. *Metals*, 7(12), Article 546. <https://doi.org/10.3390/met7120546>.
- Popescu, A. C., Delval, C., & Leparoux, M. (2017). Control of porosity and spatter in laser welding of thick AlMg5 parts using high-speed imaging and optical microscopy. *Metals*, 7(11), Article 452. <https://doi.org/10.3390/met7110452>.
- Rai, R. (2008). *Modeling of heat transfer and fluid flow in keyhole mode welding* (Doctoral dissertation). The Pennsylvania State University, USA.
- Rajulu, C. G., Krishna, A. G., & Rao, T. B. (2018). An integrated evolutionary approach for simultaneous optimization of laser weld bead characteristics. *Proceedings of the Institution of Mechanical Engineers, Part B: Journal of Engineering Manufacture*, 232(8), 1407-1422. <https://journals.sagepub.com/doi/10.1177/0954405416667431>.
- Ruan, X., Zhou, Q., Shu, L., Hu, J., & Cao, L. (2018). Accurate prediction of the weld bead characteristic in laser keyhole welding based on the stochastic kriging model. *Metals*, 8(7), Article 486. <https://doi.org/10.3390/met8070486>.
- Sánchez-Amaya, J. M., Pasang, T., Amaya-Vazquez, M. R., Lopez-Castro, J. D. D., Churiaque, C., Tao, Y., & Pedemonte, F. J. B. (2017). Microstructure and mechanical properties of Ti5553 butt welds performed by LBW under conduction regime. *Metals*, 7(7), Article 269. <https://doi.org/10.3390/met7070269>.
- Satyanarayana, G. (2020). *Thermal and fluid flow simulations in conduction mode laser beam welding of zirconium alloys* (Doctoral dissertation). Koneru Lakshmaiah Education Foundation, India.
- Satyanarayana, G., Narayana, K. L., & Rao, B. N. (2018). Numerical simulations on the laser spot welding of zirconium alloy endplate for nuclear fuel bundle assembly. *Lasers in Manufacturing and Materials Processing*, 5(1), 53-70. <https://doi.org/10.1007/s40516-018-0061-7>

- Satyanarayana, G., Narayana, K. L., Rao, B. N., Slobodyan, M. S., Elkin, M. A., & Kiselev, A. S. (2019a). Numerical simulation of the processes of formation of a welded joint with a pulsed ND: YAG laser welding of ZR-1% NB alloy. *Thermal Engineering*, 66(3), 210-218. <https://doi.org/10.1134/S0040601519030066>
- Satyanarayana, G., Narayana, K. L., & Rao, B. N. (2019b). Numerical investigation of temperature distribution and melt pool geometry in laser beam welding of a Zr-1% Nb alloy nuclear fuel rod end cap. *Bulletin of Materials Science*, 42(4), Article 170. <https://doi.org/10.1007/s12034-019-1873-6>
- Voller, V. R., & Prakash, C. (1987). A fixed grid numerical modelling methodology for convection-diffusion mushy region phase-change problems. *International Journal of Heat and Mass Transfer*, 30(8), 1709-1719. [https://doi.org/10.1016/0017-9310\(87\)90317-6](https://doi.org/10.1016/0017-9310(87)90317-6).
- Wu, J., Zhang, H., Feng, Y., & Luo, B. (2018). 3D multiphysical modelling of fluid dynamics and mass transfer in laser welding of dissimilar materials. *Metals*, 8(6), Article 443. <https://doi.org/10.3390/met8060443>.
- Xue, X., Pereira, A. B., Amorim, J., & Liao, J. (2017). Effects of pulsed Nd: YAG laser welding parameters on penetration and microstructure characterization of a DP1000 steel butt joint. *Metals*, 7(8), Article 292. <https://doi.org/10.3390/met7080292>.
- Zeng, Z., Oliveira, J. P., Bu, X., Yang, M., Li, R., & Wang, Z. (2017). Laser welding of BTi-6431S high temperature titanium alloy. *Metals*, 7(11), Article 504. <https://doi.org/10.3390/met7110504>
- Zhang, X., Li, L., Chen, Y., Yang, Z., & Zhu, X. (2017). Experimental investigation on electric current-aided laser stake welding of aluminum alloy T-joints. *Metals*, 7(11), Article 467. <https://doi.org/10.3390/met7110467>.

